Available online at www.sciencedirect.com

jmr&t Journal of Materials Research and Technology

journal homepage: www.elsevier.com/locate/jmrt

Electrochemical behavior of additively manufactured patterned titanium alloys under simulated normal, inflammatory, and severe inflammatory conditions

Aydin Bordbar-Khiabani[*], *Michael Gasik*

Department of Chemical and Metallurgical Engineering, School of Chemical Engineering, Aalto University Foundation, 02150 Espoo, Finland

ARTICLE INFO

Article history:
Received 2 May 2023
Accepted 14 July 2023
Available online 20 July 2023

Keywords:
Titanium alloys
Biomaterials
Additive manufacturing
Patterned layers
Electrochemical characterizations
Inflammatory conditions

ABSTRACT

The electrochemical behavior of a biomaterial surface in local conditions is a significant factor affecting the success of the implant placement. This is of a particular importance of metallic biomaterials which can undergo oxidation, corrosion and subsequent degradation. This study reports new data on the electrochemical behavior of additively manufactured (AM) patterned titanium alloys, analyzed after 1 and 12 h immersion in three different media mimicking normal, inflammatory and severe inflammatory conditions. Polarization study showed that corrosion resistance increases with increasing immersion time in all cases. It was found that in inflammatory condition a destructive effect on the passive layer's resistance was triggered by H_2O_2 whereas in severe inflammatory condition, albumin, lactate, and H_2O_2 all have a synergistic effect towards decreasing the corrosion resistance of patterned titanium layers. Electrochemical impedance data suggests that in the severe inflammatory condition the charged albumins are attracting to the localized pitting areas, changing diffusion transport of corrosive species at the interface of the metal/passive layer. The electrochemical tests also proven that laser-assisted patterned titanium alloys surfaces have an improved corrosion resistance in simulated solutions compared to untreated titanium of the same composition. It is suggested that new surface topography and wettability are also positive factors contributing to this improved corrosion performance in patterned specimens.

1. Introduction

Commercially pure titanium (CP–Ti, Grade 2, UNS R50400) and Ti–6Al–4V alloy (Grade 5 alloy, UNS R56400) are two among the most commonly used metallic biomaterials in medical implants devices [1,2]. They are usually deployed for hard tissue (bone) replacement because of their low specific weight, high strength, good corrosion resistance, and proper biocompatibility [3,4]. Since the nature of the implant surfaces influences the adhesion of cells to implanted biomaterials, the surface characteristics and the ability of adjusting them are

* Corresponding author.
E-mail address: aydin.bordbarkhiabani@aalto.fi (A. Bordbar-Khiabani).
https://doi.org/10.1016/j.jmrt.2023.07.113

important to ensure optimal bone-to-implant integration [5,6]. For example, it has been demonstrated that macro-pores on Ti implants surface can improve wettability, tribological performance and biological behavior [7–9]. It has also been reported that a porous surface with periodic patterns can promote early cell-to-surface interactions, including adhesion, proliferation, and metabolic activity in osteoblastic cells [10–12]. The design of specific surface patterns may also positively contribute to successful bone ingrowth into an implant by enhancing the interlocking between the biomaterial and the host bone [13,14].

Additive manufacturing (AM) is an emerging technology in the fabrication of the macro- and micro-architectural framework of metallic biomaterials both externally and internally with high flexibility and sufficient precision [15–17], comprising also various porosities and surface topographies. One of popular AM techniques is powder bed fusion (PBF), particularly laser-driven PBF (L-PBF), which was currently demonstrated to be an effective AM method for geometrically complex metallic implants, including those with periodic patterns [18,19]. There is still debate about the optimal pore size for osteointegration in porous structures of metallic biomaterials. Some sources suggest a range of 100 … 400 μm [20,21] or even 650 … 1400 μm [22], although there are other ranges too-cells were found even in the deep pores even as small as dozens of micrometers [21,23,24]. Porous titanium implants manufactured using L-PBF with pore sizes of 1000 μm in an *in vitro* study were shown a significant increase in metabolic activity and cell density compared with implants with pore sizes of 500 μm [25]. However, in another study [26] a significant improvement in cells fixation capability and *in vivo* bone ingrowth after 2 weeks were demonstrated for 600 μm pore size L-PBF-made porous titanium implant compared to structures with the average pore sizes of 300 and 900 μm.

Less attention was paid to electrochemical behavior of such implants in their reactions with body fluids, as this results in changes, sometimes drastic, over time [27]. This might be an underexplored area for AM-made titanium implants because new techniques like L-PBF create local heat affected zones and can therefore change both microstructure and local electrochemical stability of the materials. Both surface modification of the material and the selection of the corrosion media [28] are very important to mimic specific *in vivo* conditions. Commonly used options (simulated body fluids, artificial saliva, etc.) cannot sometimes adequately represent the complex environment *in loco* the implantation site [29], as the implantation of orthopedic devices usually triggers a local inflammatory response in the body [30]. This needs to be properly reflected in the media composition and reactivity analysis when measured in the laboratory. During an inflammatory response, the release of reactive oxygen species (ROS), lactic acid, hydroperoxyl radicals (HO_2), hypochlorous acid (HOCl) by leukocytes and HCl by osteoclasts causes the extracellular medium to become oxidative and acidic (pH ≈ 4–5) [31]. Subsequently, microorganisms, neutrophils, and macrophages can produce more acidic (pH ≈ 2–3) and oxidative environment surrounding an implant associated with severe inflammation [32,33]. Generally, Ti-based biomaterials are relatively corrosion resistant in normal physiological conditions due to the dense oxide layers protecting the surfaces [34]. However, it was found that CP-Ti and Ti–6Al–4V alloys indeed undergo intensive corrosion and visible surface roughening when exposed to media reflecting these inflammatory and severe inflammatory conditions [35], mimicked by the addition of H_2O_2 and HCl to a phosphate-buffered saline (PBS) solution (which itself can be ranked as a normal medium). To simulate the severe inflammatory condition, H_2O_2, calcium L-lactate hydrate (CLH), bovine serum albumin (BSA), and more HCl were added to the normal biological solution [35].

In the literature, multiple surface patterning techniques on titanium alloys have been used to enhance implant performance and sometimes also the corrosion resistance [36–38]. However, till now, there are very scarce information about regularly patterned surfaces of Ti alloys made with L-PBF method. Most of the corrosion studies performed on AM Ti implants have been conducted in normal conditions [39,40], lacking consistent reports on their performance in more complex environments corresponding to post-implantation. The main objective of this study was to perform a deeper study the electrochemical and corrosion behavior of L-PBF-made patterned CP-Ti and Ti–6Al–4V substrates under the simulated normal, inflammatory, and severe inflammatory conditions, comparing the results with previous electrochemical study on untreated CP-Ti and Ti–6Al–4V substrates [35].

2. Materials and method

2.1. *Preparation of patterned CP-Ti and Ti–6Al–4V layers*

The supplied CP-Ti (99.6% purity) and Ti–6Al–4V alloy (Al 5.5 … 6.76%, V 3.5 … 4.5% wt., Ti - balance) plates by Goodfellow Cambridge Ltd. (Huntingdon, England) were used as substrates. The plates were cut into disks with 100 mm diameter for the L-PBF machine's working platform, and rinsed ultrasonically in acetone for 10 min in order to remove surface contaminants before L-PBF process. The micromorphology of the CP-Ti (99.3% Ti), and Ti–6Al–4V (Al 5.4%, V 3.8%, Fe 0.2%, C 0.009% wt., balance Ti) powders (Merck, Germany) used for L-PBF are shown in Supplementary Fig. S1.

The computer-aided design (CAD) models of square patterns with the average lengths of ~600 μm were made with nTopology software (2020, nTopology, NY, USA). The patterned Ti layers were manufactured with optimized parameters (Supplementary Table ST1) at Btech Innovation Ltd., Istanbul, Türkiye. A 3D selective L-PBF printer (Mysint100, Sisma S.p.A., Vicenza, Italy) with a fiber laser of wavelength 1060–1100 nm, power <200 W and spot diameter of 55 μm was used to overprint CP-Ti and Ti–6Al–4V layers on flat CP-Ti and Ti–6Al–4V substrates, respectively (Supplementary video SV1), therefore producing patterned layers of the same composition as the substrate. Eleven slices of the powder were applied to reach a layer thickness of ~300 μm for both samples. The process was conducted under high purity Ar atmosphere, protecting the powder from oxidation. After L-PBF, the built parts (Supplementary Fig. S2a) were cut off into small disks with a 15 mm diameter (Supplementary Fig. S2b) by wire

electrical discharge machining, washed with water and acetone using ultrasound.

Supplementary video related to this article can be found at https://doi.org/10.1016/j.jmrt.2023.07.113

2.2. Surface characterization

The surface morphology and microstructure were observed under an optical microscopy (OM, Olympus GX71, Olympus Corp., Japan) and scanning electron microscope (SEM) with an energy dispersive spectroscopy (SEM-EDS, Hitachi TM-4000Plus-RAMI, Japan). 3D profilometry in OM was made with a dedicated software (analysisDocu, Olympus Corp., Japan) with an automatic Z-stage movement and assembling of the resulted images into the package.

The phase structure of the alloys was tested using X-ray diffraction (XRD, Philips PW3040/60, The Netherlands) with a monochromatic Cu-Kα radiation source at 40 KV and 30 mA in the range $2\theta = 20 \ldots 80^{\circ}$, using a step size of 0.02°. The wettability was determined by measuring the contact angles of 5 μL phosphate buffered saline (PBS) solution's droplet via a Theta Flex optical tensiometer (Biolin Scientific, Finland) in the sessile–drop mode. Three contact angles on different regions were measured, and the mean values and standard deviations for patterned and flat Ti samples were calculated. All wettability measurements would be performed under the same conditions of temperature and humidity.

2.3. Electrochemical measurements

Electrochemical tests like open circuit potential (OCP), electrochemical impedance spectroscopy (EIS), and potentiodynamic polarization (PDP) were used to evaluate the corrosion behavior by the three-electrode configuration with a Ag/AgCl as a reference electrode (R.E.), a graphite rod (3 mm diameter) as the auxiliary electrode, and patterned Ti substrate as a working electrode (W.E.). The electrochemical measurement procedure comprised with extra details shown earlier [35]. The simulated media for electrochemical studies with their respective compositions are summarized in Supplementary Table ST2. The post-corrosion morphologies were studied after the PDP test using SEM/EDS on surfaces immersed in simulated biological media for 12 h.

3. Results and discussion

3.1. Microstructures and chemical composition

Fig. 1 shows two-dimensional (2D) and three-dimensional (3D) OM images of the patterned layers. Fig. 1a reveals that CP-Ti layer is patterned squarely with an average window size of about 610 μm in diameter. Similarly, the printed Ti–6Al–4V pattern (Fig. 1c) revealed square columns with a side length of ~560 μm and a strut size of ~500 μm. It can be seen that the average window size in both patterned samples is between 500 … 600 μm, which might be considered close to the optimal values reported in other studies [23,24,41]. There are some differences between the CP-Ti and Ti–6Al–4V printed surfaces. In the patterned CP-Ti sample, the size of the strut was higher compared to sample Ti–6Al–4V, and the height profile of the strut branch has become a stair-step.

Since the laser beam has a Gaussian distribution profile, the powder (partially melted by laser) occupies more space near well boundaries than what is predicted by ideal model

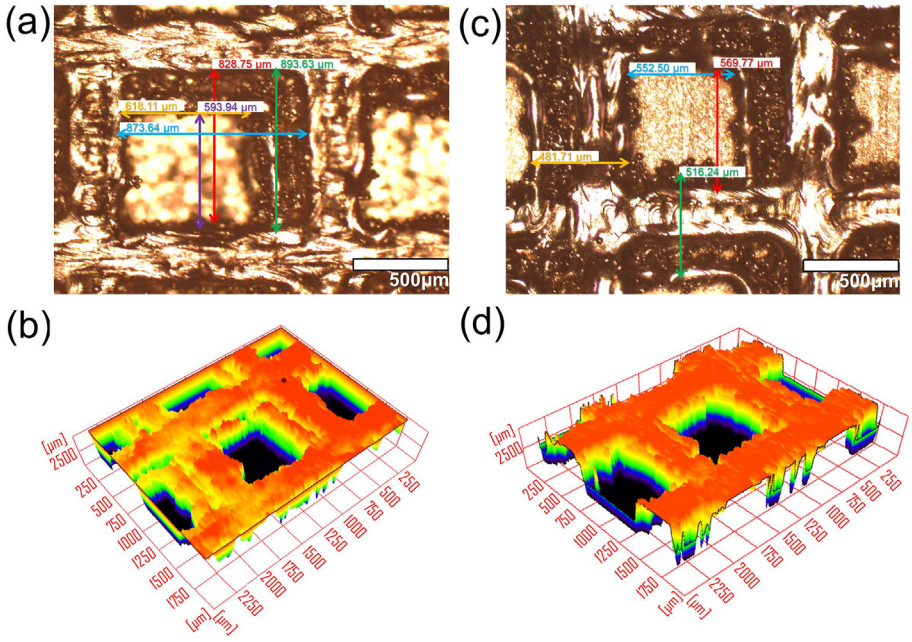

Fig. 1 – The 2D and reconstructed 3D OM images of patterned (a, b) CP-Ti and (c, d) Ti–6Al–4V (grid size = 250 μm). For b) and d) note vertical z-scale number shows the absolute specimen position during scanning and not the depth of the patterned wells.

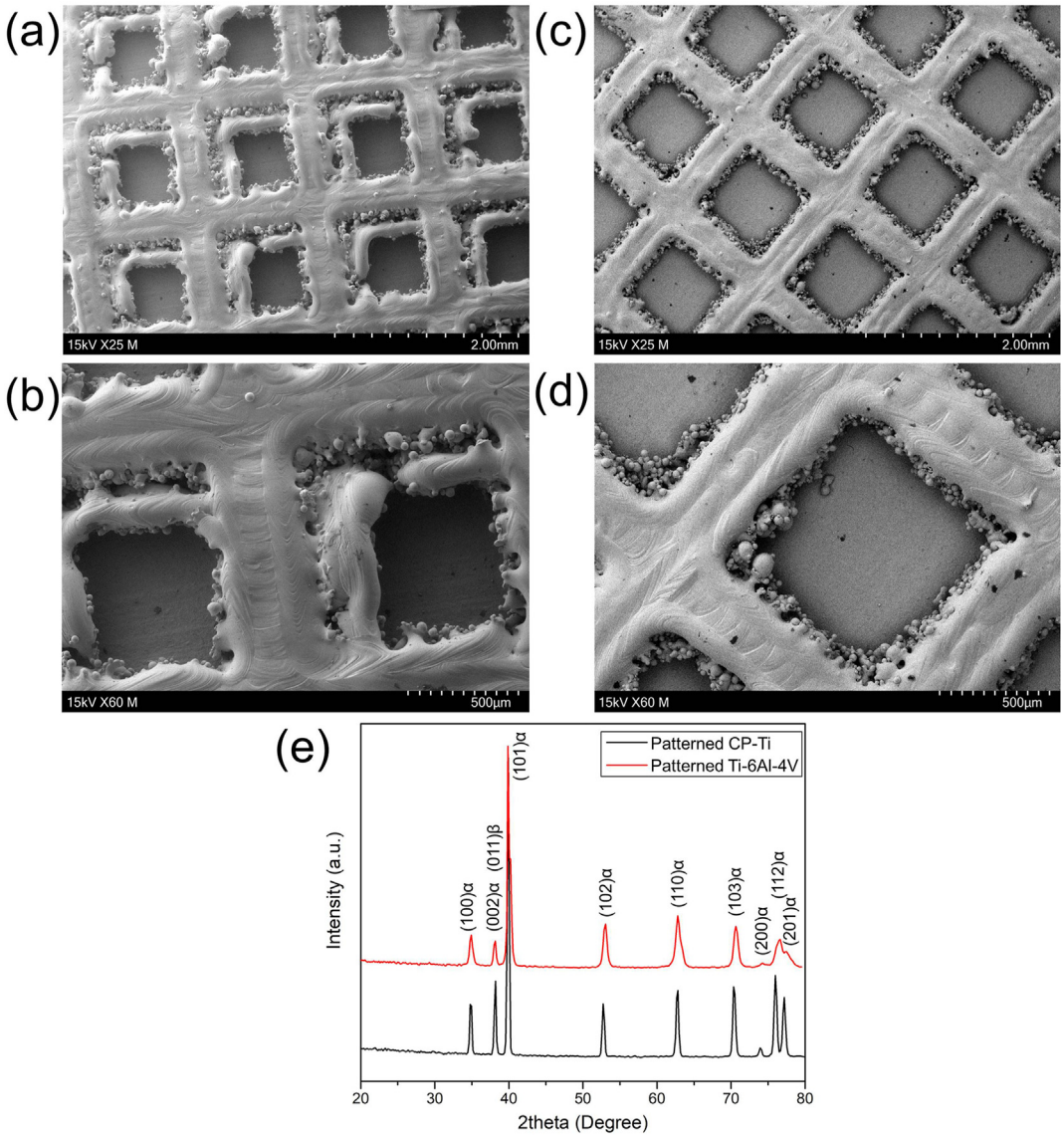

Fig. 2 – The top-surface SEM micrographs of patterned (a, and b) CP-Ti and (c, and d) Ti–6Al–4V layers in different magnifications; (e) XRD patterns of patterned CP-Ti and Ti–6Al–4V layers.

made with CAD. The difference between the sizes of the struts in the two samples can be related to the size of the powders, as explained in Supplementary Fig. S3a. The laser beam provided in the L-PBF machine (55 μm) possesses the highest intensity near the center and decreasing outward (Supplementary Fig. S3b). CP-Ti powders used in this study has dimeter ~20 μm, so the central region that had a better beam intensity. The CP-Ti powder particles would melt within this 20 μm space and be better attached to the edges of the patterns, resulting in more particles being able adhere to the edges leading to a wider strut than the one obtained with Ti–6Al–4V powder (~50 μm size).

SEM images of the top surface of the patterned CP-Ti and Ti–6Al–4V layers are shown in Fig. 2a–d in two magnifications. They show that the regular square patterns with a complete strut are distributed on the top surface of samples. The surface of the patterned samples has a large number of small spherical particles (Fig. 2c and d). These particles are very similar in size and shape to as-received CP-Ti and Ti–6Al–4V powders (Supplementary Figs. S1 and S2). Attached metallic particles on the lattice strut surfaces are originating from the complete or partial melting of each layer of bent struts with different inclined angles, followed by adherence to the strut surface with diffusion [42,43]. The EDS maps and spectra for corresponded areas of patterned CP-Ti and Ti–6Al–4V (Supplementary Fig. S3a and Fig. S3b) show that the patterned Ti–6Al–4V layers constitute of Ti, Al, and V and small amounts of oxygen. The printed layer composition was consistent with the original composition of Ti–6Al–4V powders (Ti 90%, Al 5.4%, V 3.8%, Fe, O, C < 1% wt.), indicating that laser-powder interaction did not cause changes in alloying elements concentration during L-PBF. The EDS maps of patterned Ti–6Al–4V are characterized by solid solution alloying elements without non-homogeneous precipitates. It

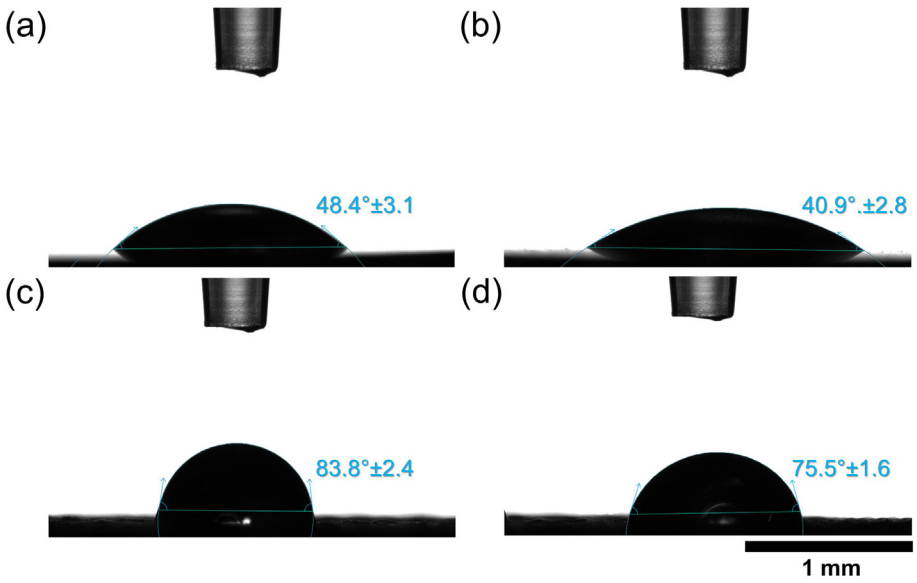

Fig. 3 – The PBS solution droplet contact angle for the flat (a) CP-Ti and (b) Ti–6Al–4V surfaces; and for the patterned (c) CP-Ti and (d) Ti–6Al–4V surfaces. In patterned surfaces, the droplet covered one-two wells.

indicates that during the L-PBF process, the melted metallic particles have solidified under fast cooling rates without segregation.

Fig. 2e represents the XRD profiles of the surface of patterned CP-Ti and Ti–6Al–4V layers on the same substrates. For both printed samples, the α-Ti peaks were identified using the reference cards JCPDS file #44–1294, and no oxide-related peaks were observed. The peak at $2\theta = 39.5^{\circ}$ in the graph of the printed Ti–6Al–4V layers shows a combination of α- and β-phase. Generally, due to the rapid cooling process used in the L-PBF production of Ti–6Al–4V alloys, only a small amount of the β-phase remains and thus it is difficult to detect the β-phase in Ti–6Al–4V alloys using XRD patterns in the vast majority of L-PBF cases [44,45].

3.2. *Surface wettability*

The surface wettability of titanium implant materials significantly influences corrosion behavior, protein adsorption, and cell adhesion [46]. Fig. 3 shows the results of an experiment evaluating the wettability of flat and patterned Ti samples based on the contact angle goniometry of a PBS solution's droplet. Surfaces that have a contact angle less than 90° are commonly classified as hydrophilic, otherwise, they are hydrophobic. All samples considered in this study were found to be hydrophilic according to this criterion: the contact angle values increased from 48.4 ± 3.1° for the flat CP-Ti surface to 83.8 ± 2.4° for the patterned sample, and from 40.9 ± 2.8° for the flat Ti–6Al–4V surface to 75.5 ± 1.6° for its patterned sample. This is expected, as surface roughness influences the wettability behavior of surfaces according to the Wenzel and Cassie-Baxter models. Similar contact angle values for flat Ti–6Al–4V to PBS solution have been reported by other studies [47].

In this study, contact angle values could have increased by coupled effects of increasing surface roughness and air pockets trapped beneath the PBS droplet which is well justified using principal Cassie–Baxter's theory. Nevertheless, the patterned surfaces were still hydrophilic in nature. It has previously been reported that Ti-based implants manufactured using L-PBF process might have a hydrophilic surface [48,49]. The noticeable variations in the contact angle values of patterned specimens could be related to a geometrical dissimilarity between the CP-Ti and Ti–6Al–4V patterns, especially in struts morphology. The surface chemical composition also influences wettability. It has been reported that the Ti–6Al–4V surface makes lower contact angle than CP-Ti due to the presence of aluminum and vanadium oxides on its surface [50,51].

3.3. *Electrochemical studies*

3.3.1. *Open circuit potential*

Data on OCP variations of patterned CP-Ti and Ti–6Al–4V layers after 1 and 12 h of immersion in simulated media are shown in Fig. 4. OCP values move toward electropositive potentials in the simulated inflammatory and severe inflammatory environment after implantation. A possible explanation for this is the decomposition of H_2O_2 into H_2 and O_2, thereby serving as an additional cathodic reaction in a sluggish oxygen reduction reaction [52]. Earlier studies indicate that the positive OCP values in inflammatory solutions can be attributed to the adsorption of oxidizing intermediates, such as $\cdot HO_2$ and $\cdot HO$, onto the passive film on Ti-based biomaterials [53]. In severe inflammatory conditions, adding BSA and CLH to the inflammatory solution (H_2O_2+PBS) decreases OCP values. Nevertheless, OCP values remain higher and more positive than normal conditions (PBS).

BSA presented in media adsorbs on the surface of Ti by chemisorption through carboxylate/amino functional groups or electrostatic interactions, inhibiting oxygen reduction reactions [54], resulting in decreasing surface potential. CLH

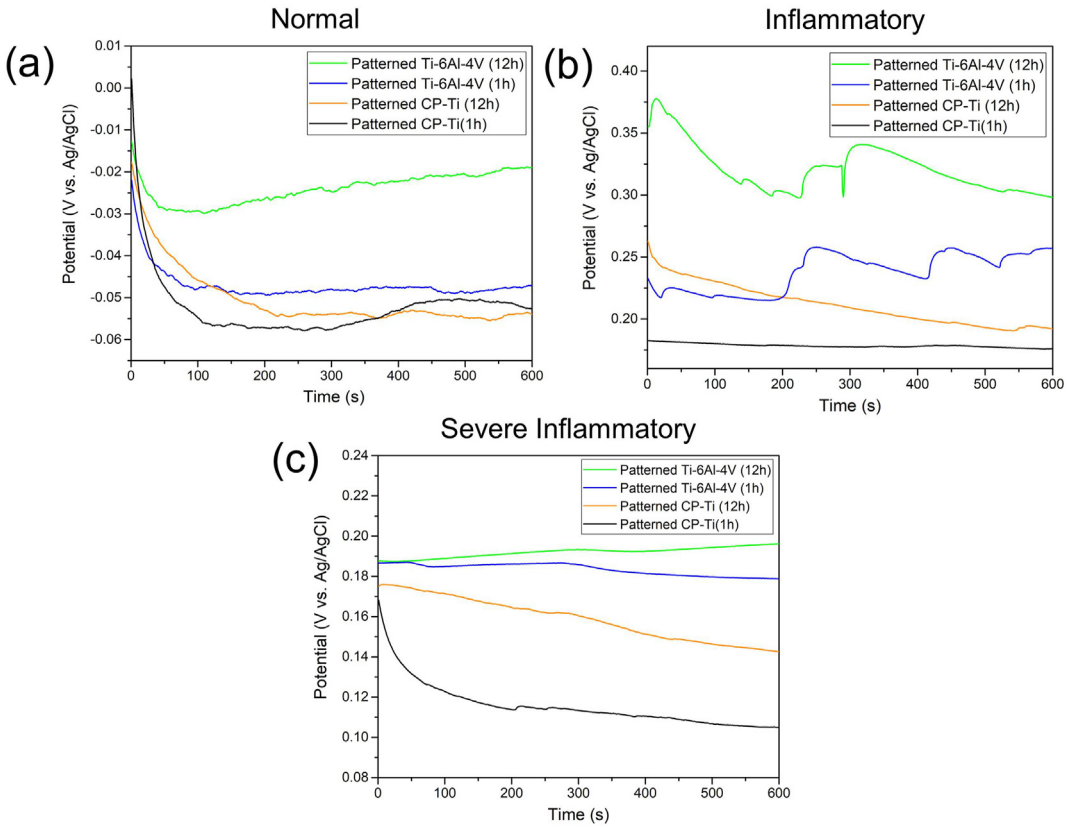

Fig. 4 – OCP monitoring of the patterned CP-Ti, and Ti–6Al–4V layers exposed in simulated (a) normal, (b) inflammatory, and (c) severe inflammatory conditions for 1 h and 12 h.

adsorption on the surface of Ti implants also significantly blocks the cathodic site in H_2O_2-containing solutions, giving a lower OCP value [55]. It can also be observed that under all conditions with increasing immersion time, OCP values increased. Due to suppressed anodic reactions anodic current density has decreased and passive oxide layers have chemically reconstructed or thickened [56]. The patterned Ti–6Al–4V layer shows a much higher potential than patterned CP-Ti layer under all conditions, which is likely to be due to the formation of a passive layer which may have also aluminum and vanadium oxides, being also denser than the pure oxide layers present on CP-Ti [1,2]. H_2O_2 may cause fluctuations in the OCP evolution of patterned Ti–6Al–4V layer in an inflammatory environment due to the high resistance of the passive layer [52]. Fig. 4 also revealed that the patterned specimens had different OCP values compared with flat counterpart specimens (OCP evolutions for flat CP-Ti and Ti–6Al–4V were reported in our previous study [35].). In patterned specimens, OCP shows more of a shift towards electropositive values under normal and inflammatory conditions compared to flat Ti substrate, whereas OCP values do not change much in severe inflammatory conditions.

3.3.2. *Potentiodynamic polarization*

Fig. 5 shows the potentiodynamic polarization (PDP) plots for patterned CP-Ti and Ti–6Al–4V layers after different immersion times in simulated normal, inflammatory and severe inflammatory solutions. Based on Tafel extrapolation from cathodic and anodic branches of the polarization curves, corrosion potentials (E_{corr}) and corrosion current densities (I_{corr}), Tafel slopes of anodic (β_a) and cathodic (β_c) branches were obtained. The polarization resistance (R_p) was calculated using the Stern-Geary Equation [57]:

$$R_p = \frac{\beta_a \beta_c}{2.3 i_{corr}(\beta_a + \beta_c)} \quad (1)$$

The values of E_{corr}, β_a, β_c, I_{corr}, and R_p extracted from the plots are summarized and compared with previous study in Supplementary Table ST3. As seen in Fig. 5a and b, all patterned specimens display passivation behavior in anodic branches after 1 h and 12 h immersion under normal conditions. This behavior is consistent with the literature [58]. However, the presence of H_2O_2 in the inflammatory and severe inflammatory solutions, has prevented specimens from exhibiting passive behavior under these conditions [59]. Hence anodic branches do not exhibit Tafel behavior [60], making it impossible to obtain accurate measurements of anodic Tafel slopes (β_a) meaning the Stern–Geary analysis became invalid.

The I_{corr} values were increased after adding the H_2O_2 to the PBS for all specimens, indicating higher corrosion rates during inflammation (Supplementary Table ST3). For the inflammatory condition compared to the normal condition, the E_{corr} values were electropositive, similar to the OCP values in

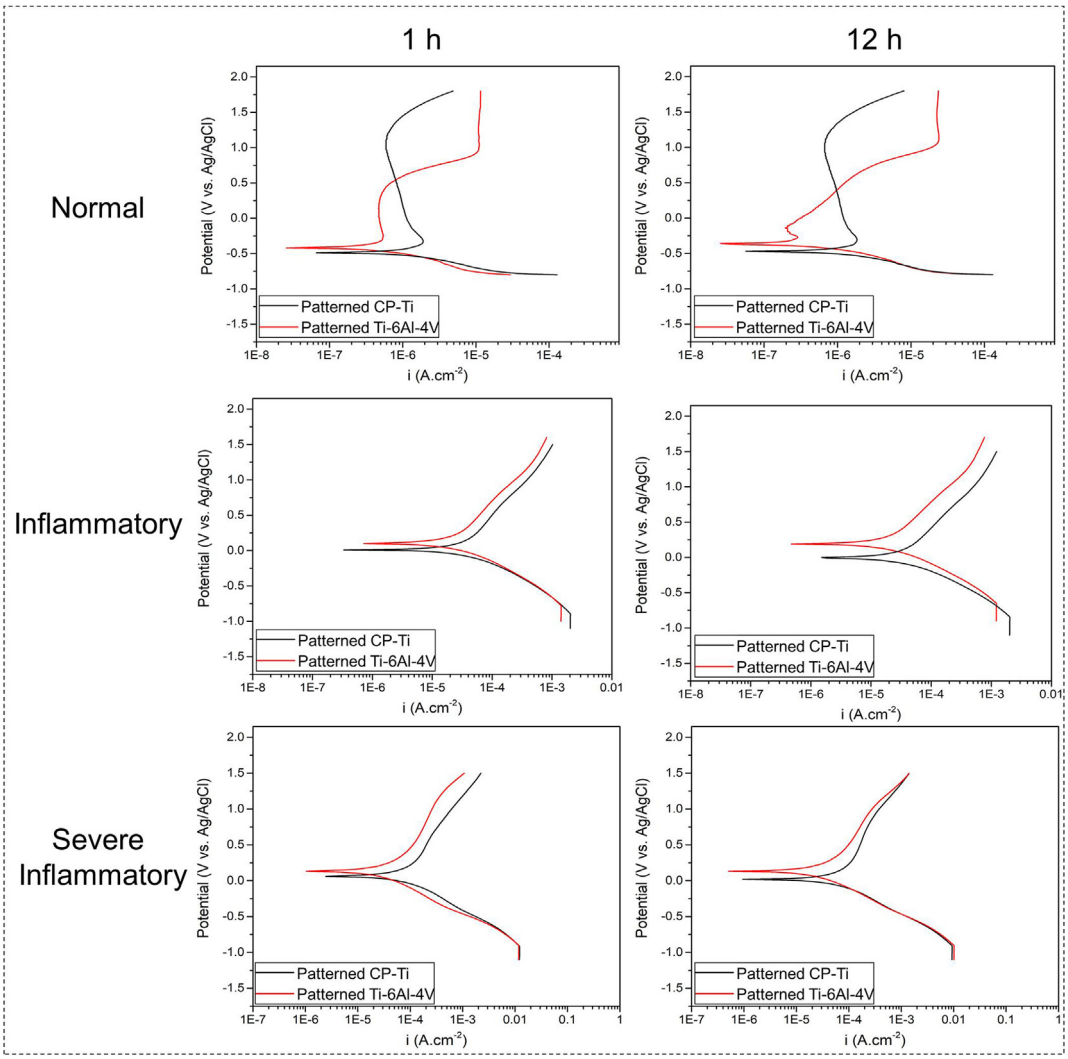

Fig. 5 – PDP curves of the patterned CP-Ti and Ti–6Al–4V layers exposed in simulated normal, inflammatory and severe inflammatory conditions for 1 and 12 h.

Fig. 4b. This corrosion behavior is consistent with previous studies of H_2O_2-containing biological solutions. A combination of BSA, CLH, and H_2O_2 in PBS (severe inflammatory media) result in an increase of I_{corr} and a decrease in R_p, suggesting a synergetic action of these compounds on the corrosion behavior of patterned Ti specimens.

From the point of view of immersion times' effect on electrochemical behavior, it can be said that the Icorr and Rp values have decreased and increased respectively in all conditions after 12 h of immersion. It can be explained by the formation of a stable protective oxide film in the normal condition that protects patterned materials' surfaces from further damage. H_2O_2 undergoes catalytic decomposition into H_2O and O_2 a prolonged immersion times during severe inflammatory and inflammatory conditions, thus reducing the oxidizing power of the solutions in these cases. In both inflammatory conditions, I_{corr} values for patterned CP-Ti specimens exhibits a gradual increase, indicating that the implant surface oxidizes when exposed to H_2O_2-containing solutions [61]. Nevertheless, the formed oxide dissolves more quickly than is necessary for optimal protection.

The patterned Ti–6Al–4V layer demonstrated superior corrosion resistance than patented CP-Ti under all simulated conditions, which correlates with other data [62]. When inflammation and severe inflammation conditions were present, I_{corr} of patterned Ti–6Al–4V specimens increased as compared to normal conditions. As a result of vanadium oxides (VO_2, V_2O_4, V_2O_5) dissolving in the native oxide layer on the Ti–6Al–4V alloy under inflammatory conditions described in the literature, cation vacancies are generated in the passive film, resulting in an increase in I_{corr} [62,63]. It is further enhanced by the presence of H_2O_2 molecules, lactate and chlorine ions. It is not straightforward to describe how BSA and CLH influence the corrosion process of patterned Ti6Al4V layer, as they can have an effect on both anodic and cathodic reactions [54].

It has been reported that the BSA and CLH can accelerate corrosion through their effect on the dissolution of the oxide on the Ti–6Al–4V alloy through anodic reactions. As a result of the generation of soluble complexes like metal-biomolecule matrices, the available metal ion species in the oxide passive layer will be consumed and the passive film dissolution will be

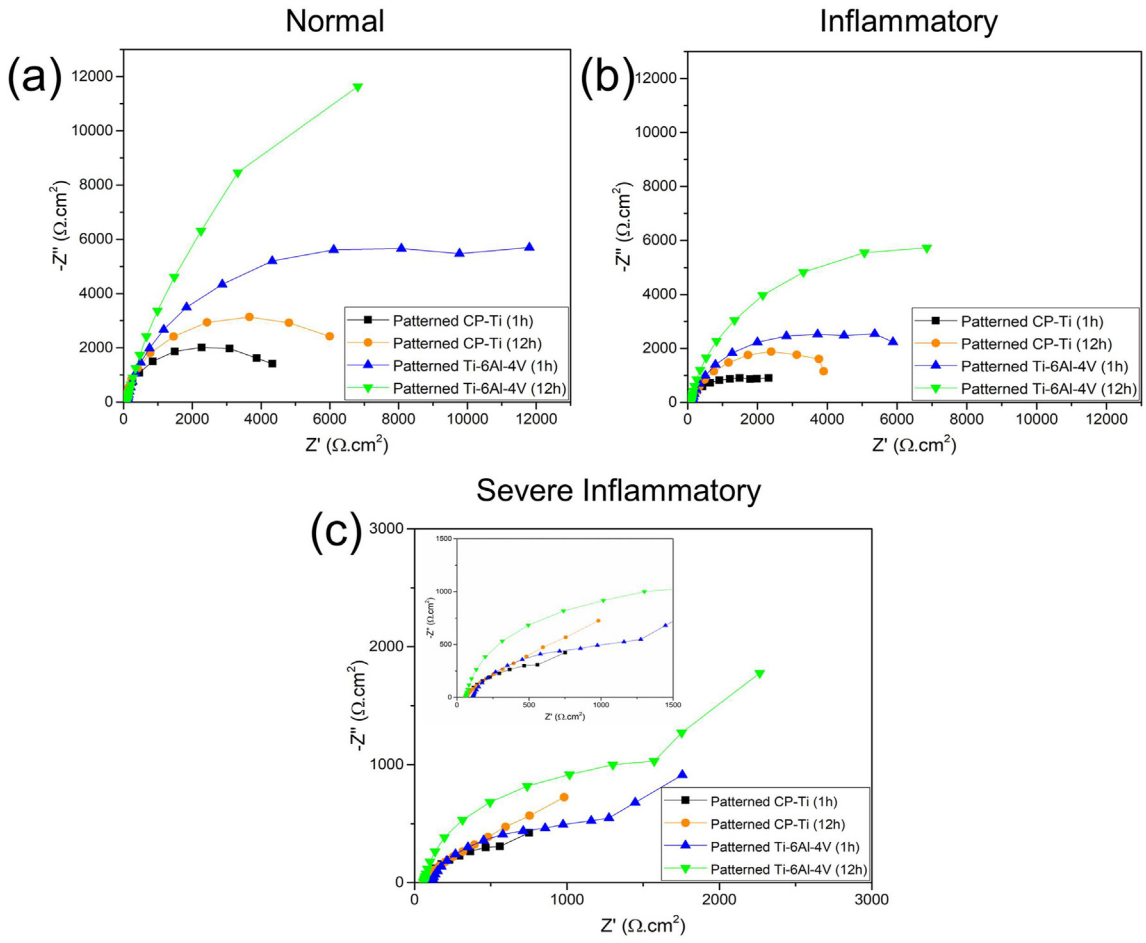

Fig. 6 – EIS plots of the patterned CP-Ti and Ti–6Al–4V layers exposed in simulated normal, inflammatory and severe inflammatory conditions for 1 and 12 h: (a–c) Nyquist plots. Nyquist plots for the severe inflammatory condition have been enlarged for better display.

accelerated, which may be a major cause of the expedited anodic reaction kinetics associated with the co-existence of CLH and BSA biomolecules [54,55]. When comparing the I_{corr} of patterned layers with the results obtained from the previous study on flat specimens, it is evident that in both cases of Ti–6Al–4V and CP-Ti, the patterned specimens have a lower I_{corr}, indicating better corrosion performance of them in all simulated conditions. The lower I_{corr} of patterned Ti layers can be attributed to a number of factors arising from the surface topography difference induced by the L-PBF process.

The beneficial influence of periodic patterns on the corrosion response of Ti implants was observed in earlier studies [36,37]. As seen in Fig. 3, creating square patterns on the surface of flat substrates increases the contact angle. Indeed, patterned samples had a relatively higher contact angle (Fig. 3), which resulted in fewer tendencies to absorb water molecules on the surface, leading to a high corrosion resistance. Consequently, aggressive ions reach the substrate at a slower rate and the substrate is less exposed to corrosive media and agents. It has also been established that Ti6Al4V implants fabricated through the L-PBF process exhibit a lower I_{corr} and a nobler E_{corr} in biological solutions when compared to wrought counterparts [60,64,65].

3.3.3. *Electrochemical impedance spectroscopy*

Figs. 6 and 7 present the Nyquist and Bode modulus/phase plots of EIS tests. In Nyquist plots, the diameter of capacitive semicircles decreases when H_2O_2 and HCl are added to PBS, which indicates that corrosion resistance, is deteriorating under the inflammatory condition. When BSA and LCH are introduced into the medium of severe inflammatory conditions, the diameter of semicircles decreases sharply, indicating a drastic reduction in corrosion resistance [54,55]. The patterned Ti–6Al–4V exhibits nobler electrochemical behavior than patterned CP-Ti in all conditions, as evidenced by the largest area of capacitive semicircles and highest modulus values at low frequency (Figs. 6 and Fig. 7a–c). Phase angles of about 40° and 60° in Fig. 7f for patterned specimens implies almost complete destruction of passive film under severe inflammatory conditions. The EIS data is analyzed using equivalent circuits shown in Supplementary Fig. S5. In both circuits, R_s represents the resistance of the corrosion test solution between the R.E. and W.E. The circuit in Supplementary Fig. S5a was used for fitting the data obtained in normal and inflammatory conditions and it contained the constant phase element of the passive layer parallel with the resistance of the passive layer (CPE_{pl}/R_{pl}). A constant phase

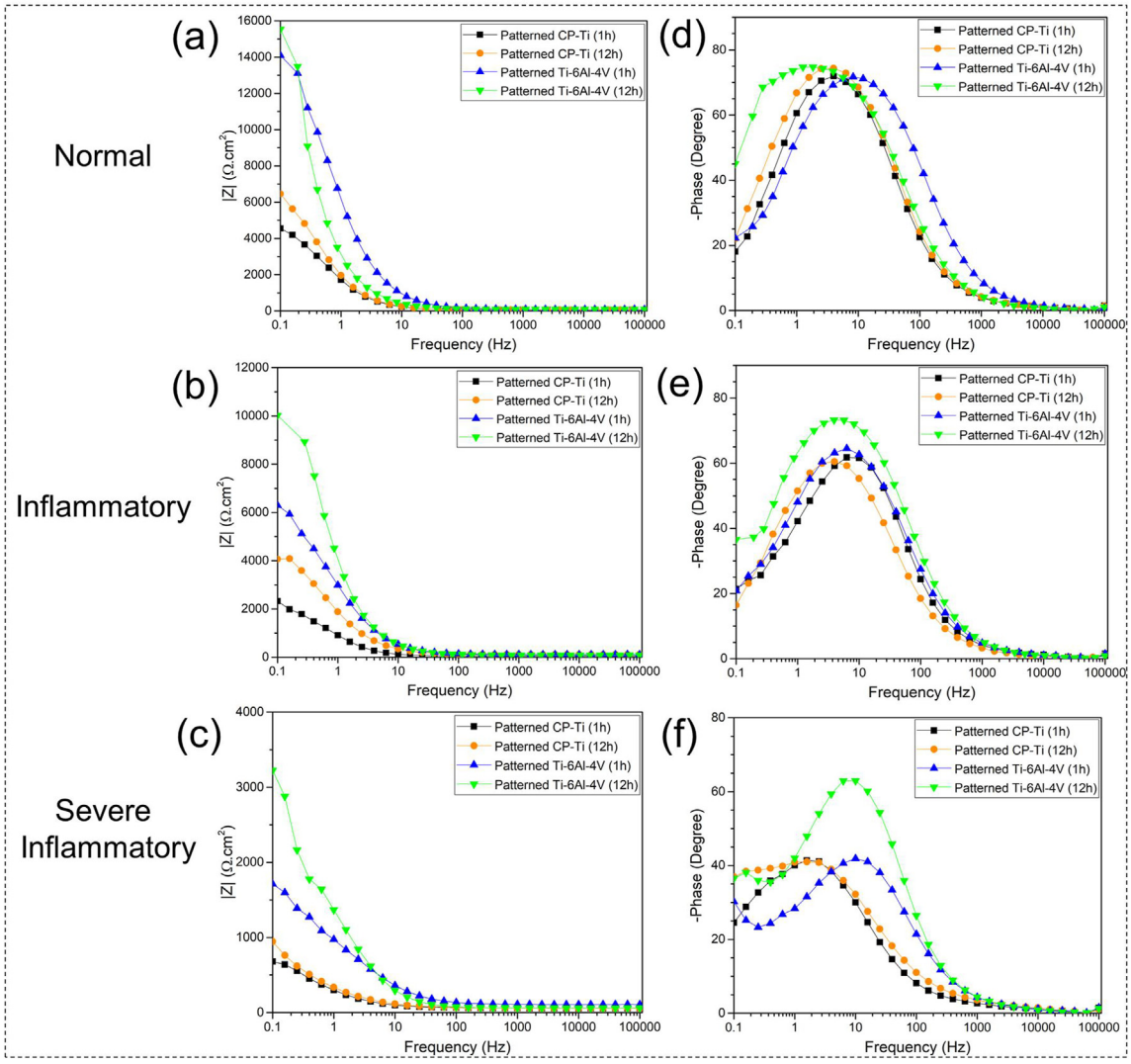

Fig. 7 – EIS plots of the patterned CP-Ti and Ti–6Al–4V layers exposed in simulated normal, inflammatory and severe inflammatory conditions for 1 and 12 h: (a–c) Bode modulus, and (d–f) Bode phase plots.

element (CPE) formalism is applied to express the capacitive characteristics of coating surfaces due to the "scattering effect" resulting from the nonhomogeneous nature of the passive layer's surface [66]:

$$Z_{CPE} = \frac{1}{Q(j\omega)^n} \quad (2)$$

where $j^2 = -1$, ω is an angular frequency (rad.s^{-1}), and $n = 0 \ldots 1$ is the power coefficient (with n = 1, CPE behaves as a pure capacitance, and for n = 0 as a pure resistance). The value of Q is usually used to approximate interfacial capacitance, but this approach does not always consistently work [66]. The effective capacity (C_{eff}) for each passive layer was calculated using the Brug model [67]:

$$C_{eff} = \sqrt[n]{Q \cdot R_T^{1-n}} \quad (3)$$

where R_T is the total resistance sum ($R_{ct} + R_{pl}$). The passive layer thickness (d_{eff}) can be estimated using the equation [68] as follows:

$$d_{eff} = \frac{\varepsilon \varepsilon_0}{C_{eff}} \quad (4)$$

where ε is the relative permittivity of the material (around 45 for TiO_2 passive film [68]), and ε_0 is the vacuum permittivity (8.85×10^{-14} F cm^{-1}). As seen in Supplementary Fig. S5b, the circuit for severe inflammatory solution contains two-time constants and a Warburg component due to the difference in impedance characteristics. Here the capacitance of the electrical double layer at the interface between the substrate and solution is denoted by CPE_{dl} and the resistance to charge transfer is shown by R_{ct} [69]. As a phase element, Warburg open terminus (W_o) demonstrates semi-infinite length diffusion of corrosion ions across the passive layer [70]. A straight line at an angle of 45° appears at the low-frequency region of the Nyquist plots in the severe inflammatory condition (Fig. 7c). This can be attributed to the Warburg impedance formed at this frequency [70]. It was found that the best fit to the data was achieved with the W_o element connected in

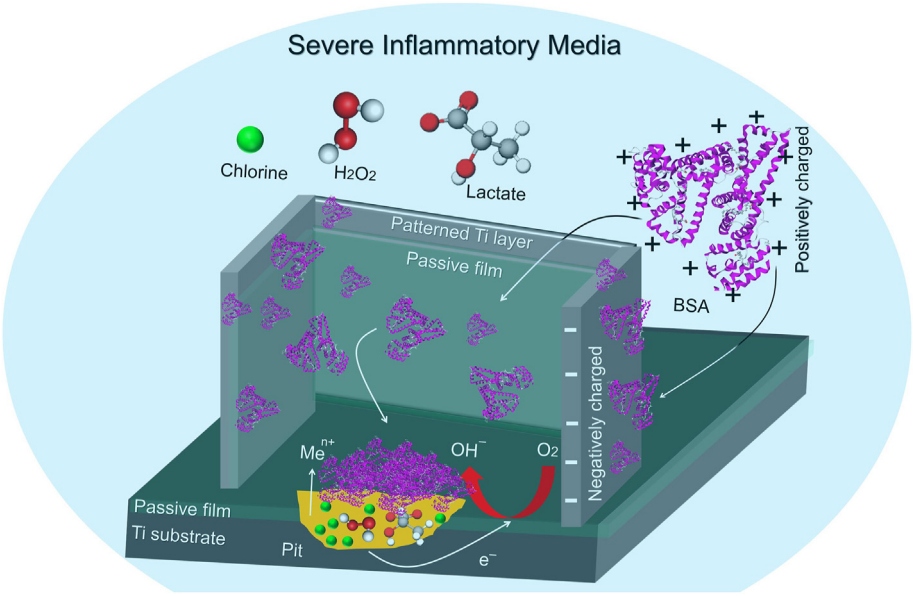

Fig. 8 – Schematic representation of the corrosion mechanism for patterned Ti layers in the severe inflammatory media.

series with the R_{ct}. W_o element can be expressed mathematically as follows [71]:

$$Z_{W_o} = \frac{W_{o-R} \cdot \coth\left[(W_{o-t} \cdot j\omega)^{W_{o-P}}\right]}{(W_{o-t} \cdot j\omega)^{W_{o-P}}} \quad (5)$$

where $W_{o\text{-}R}$ and $W_{o\text{-}t}$ correspond to the Warburg pseudo-resistance and diffusion time, respectively. The $W_{o\text{-}P}$ represents the power coefficient varying as 0 … 1. In the diffusional process assumes that characteristic time $W_{o\text{-}t} = \delta^2/D_{diff}$, where δ is the diffusion layer thickness and D is the effective diffusion coefficient of the corrosive ions.

The fitted results of EIS and computed values by equations (1)–(4) are itemized in Supplementary Table ST4 and the values of each individual parameter of Warburg elements in Supplementary Table ST5. All R_{pl} values for patterned specimens decreases under inflammatory and severe inflammatory conditions, indicating that corrosion resistance is weakening. The reaction between Ti and H_2O_2 results in the formation of the less stable Ti(IV)–H_2O_2 complex compounds, which do not offer a high level of resistance against corrosive agents [56]. This lower compactness of the passive film is reflected in the higher CPE_{pl} [66]. Much higher values of CPE_{pl} in the inflammatory and severe inflammatory solutions indicate further drop in corrosion resistance. When a specimen exposed to H_2O_2-containing strong acidic solutions, the passive film is damaged, causing the surface to dissolve more and increasing the cathode reaction rate [52].

Values of R_{pl} in the severe inflammatory have been noticeably decreased compared to inflammatory conditions, showing a synergetic behavior of both CLH and BSA on patterned Ti layers degradation [54,55]. It was recently reported that biomolecules in the active layer are aligned to produce an electric field throughout the passive layer due to ROS intermediates' high oxidation potential [72]. It is also possible CLH produces a lactate-chelating compound with Ti that would explain a decrease in R_{pl} during severe inflammation [73]. All specimens displayed an increase in R_{pl} after 12 h in all conditions, indicating that a passive protective film was forming and growing, facilitating the self-healing of passive layers in inflammatory media including the effect of the decomposition of H_2O_2 to H_2O and O_2 [52]. The rate of metal dissolution with the broken passive film is generally related to the R_{ct} and here it is seen that R_{ct} for patterned Ti–6Al–4V is slightly larger than that for patterned CP-Ti for both immersion times. Therefore, patterned Ti–6Al–4V layers display better corrosion protection performance than patterned CP-Ti layers on their own substrates in the severe inflammatory solution [62].

Supplementary Table ST4 shows that the surface patterning has effectively improved the corrosion resistance of the flat specimens in all simulated media. A lower CPE_{pl} of patterned Ti layers than flat Ti specimens indicates that the passive film that forms over patterned layers has a lower defect density. $W_{o\text{-}R}$ values rise in patterned Ti–6Al–4V layers under severe inflammation (Supplementary Table ST5) as a result of the formation of strong oxide layers, as reported [74,75] for CP-Ti and Ti–6Al–4V corrosion in HCl-based fluids. Both $W_{o\text{-}R}$ and $W_{o\text{-}t}$ values are likely to increase with immersion time due to the increased penetration pathway of electrolyte through a thicker passive layer.

The equivalent circuit proposed for patterned specimens under severe inflammatory conditions (Supplementary Fig. S5b) differs from the circuit previously reported in our study for fitting EIS plots of flat Ti–6Al–4V and CP-Ti specimens under the same condition [35]. The Warburg impedance and R_{ct} indicates that diffusion of corrosive ions across the interface between the passive layer and the patterned substrate is responsible for electrochemical reactions in severe inflammatory condition [70]. Indeed, patterned layers on the surface Ti have caused a change in the corrosion mechanism compared to flat Ti in the severe inflammatory environment.

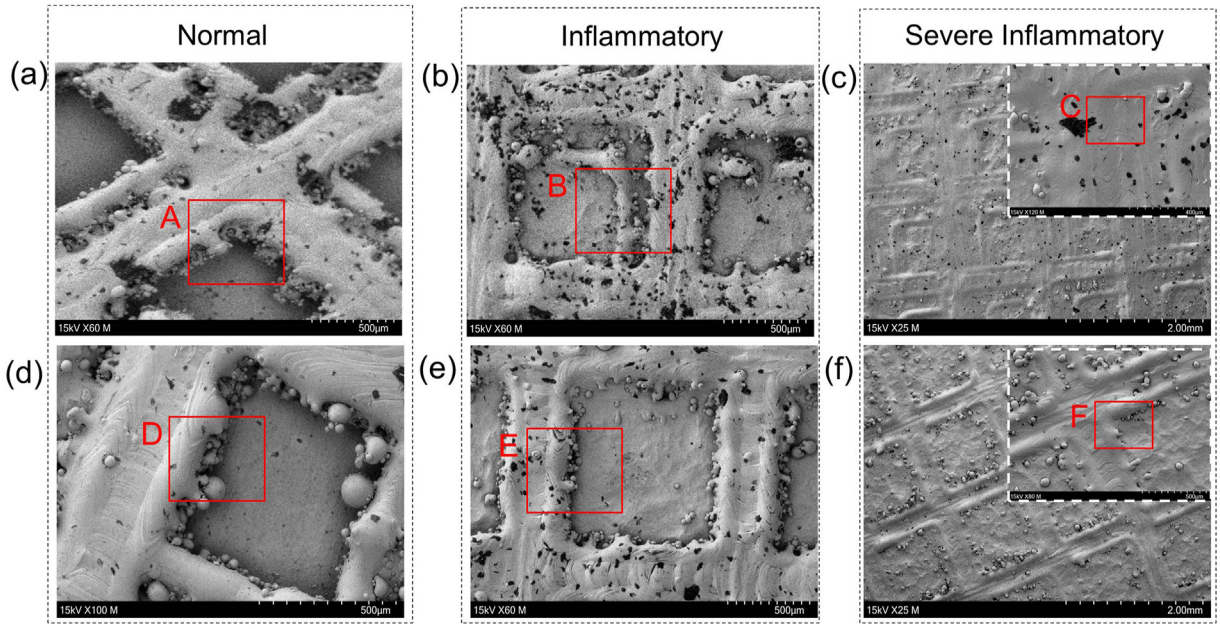

Fig. 9 – Top-surface SEM micrographs of patterned specimens exposed in simulated normal, inflammatory and severe inflammatory conditions for 12 h: (a–c) CP-Ti, and (d–f) Ti–6Al–4V. SEM micrographs for the severe inflammatory condition have been shown in different magnifications.

The proposed corrosion mechanism for patterned Ti layers under the severe inflammatory condition is schematically illustrated in Fig. 8 where the cross-sectional view of a square printed pattern on the Ti substrate is shown. The gradient in oxygen concentration between the exterior and interior parts of the square patterned wells results from the hindered mass transport process within these struts. This gradient leads to an inferior surface potential of internal parts than at the outside parts, so more metallic ions are released and accumulated at the interior due to the anodically polarized Ti surface in localized corrosion pits. On the other hand, electron transfer to the outer part of the pit causes the cathodically polarized outer parts of the struts.

Taking into account that BSA is positively charged in the severe inflammatory condition at pH ≈ 3 [76], migration of positively charged BSA into the exterior part of the localized pit is essential in order to maintain charge balance. Larger amount of BSA hence accumulates in the outer parts, possessing higher electric charge on sharp and rough structures, with their number gradually increasing with the immersion time. BSA adsorption can also be further enhanced by the surface potential difference [77]. Additional negative charges are also generated by the potential difference between the exterior and interior of the corrosion pit, enabling them to interact with positive BSA particles, promoting their adsorption onto the alloy surface within the interior parts the localized corrosion regions [78]. In the vicinity of corrosion pits, BSA absorption and accumulation affect the penetration and interaction of corrosive agents across the passive layer and the impedance response exhibits the unique Warburg impedance characteristic. Additionally, Cl^- ions in the solution can trap under a mass of BSA particles near the broken passive film to form a charge transfer and an electric double layer [79].

3.3.4. *Surface morphology after PDP tests*

SEM images and corresponding EDS spectra for the morphologies of patterned specimens after PDP in different conditions tests are shown in Fig. 9 and Supplementary Fig. S6. The PDP test of patterned Ti materials after 12 h immersion generally resulted in selective dissolution, pitting occurrence, and passivation decomposition. It can be seen in Fig. 9a that patterned CP-Ti layer is susceptible to inferior pitting corrosion under normal condition. However, fewer pits and localized corrosion products are detectable on the patterned Ti–6Al–4V surface in same conditions (Fig. 9d). Compared to the normal conditions, severe inflammatory and inflammatory conditions show a decrease in Ti and an increase in O (Supplementary Fig. S6), indicating a higher growing the oxide film over immersion time for the both patterned layers.

Lots of wide and deep pits can be seen on the struts surface in inflammatory condition (Fig. 9b), indicating the degradation of patterned CP-Ti layer in the presence of H_2O_2 and Cl^- ions [80]. The Cl^- accumulation at the surface of localized corrosion regions leads to rupture of the oxide film (Supplementary Fig. S6b): when Cl^- ions are adsorbing on oxygen vacancies on the surface of a metal oxide in the presence of H_2O_2, they are produced extra cation vacancies. The condensation of excessive cation vacancies facilitates the formation of pit nuclei [81]. According to Fig. 9b and e, pits seem to propagate along non-melted particle interfaces at different rates and in various directions, starting from a local defect on patterned surfaces (void). It has been noted [82] that pits tend to form in areas with a high residual tensile stress in porous Ti materials produced by L-PBF.

The patterned Ti specimens under the severe inflammatory condition were covered almost completely with corrosion products. The original morphology of these specimens,

however, can still be observed. It is seen from Fig. 9c that numerous corrosion pits are randomly distributed on the corroded surface of patterned CP-Ti, and the number of which is significantly higher than patterned Ti–6Al–4V (Fig. 9f). The presence of more carbon in regions "C" (Fig. 9c) and "F" (Fig. 9f) correlates with the envisaged CLH and BSA adsorption to patterned Ti layers under the severe inflammation [55,73,83].

4. Conclusions

In this work, the authors have studied the electrochemical corrosion behavior of AM-patterned CP-Ti, and Ti–6Al–4V layers under simulated normal, inflammatory, and severe inflammatory conditions. The electrochemical stability of patterned layers was evaluated by OCP, PDP, and EIS tests. This study has drawn the following main conclusions:

(1) The patterned CP-Ti layer showed different morphology with stair-step struts compared with patterned Ti–6Al–4V alloy. It was attributed to the difference in the size of powders with the laser beam diameter.
(2) The wettability results suggest that the PBS droplet's contact angles were increased on AM-patterned Ti layers compared with their flat counterparts, but hydrophilic behavior has remained.
(3) The OCP monitoring shown values moving towards the nobler direction with the increase of immersion time and it is explained by an increase in the passive layer's thickness under normal conditions with the decomposition of H_2O_2 during inflammatory and severe inflammatory conditions.
(4) The PDP results showed that the I_{corr} values of the patterned layers is increased in the order: normal < inflammatory < severe inflammatory, indicating the role of H_2O_2, BSA, and CLH in destruction of the passive layer.
(5) The equivalent circuit scheme obtained under the severe inflammatory condition differs from normal and inflammatory conditions, which is connected with altered corrosion mechanism when charged albumins are attracted to the localized pitting areas. There they cause the diffusion of corrosive species controlling the electrochemical process at the interface between the metal and the passive layer.
(6) The PDP and EIS tests indicated that patterned Ti–6Al–4V layers had better electrochemical performance under all conditions than the patterned CP-Ti. SEM micrographs also confirmed that the pitting tendency of patterned CP-Ti layers was higher than the patterned Ti–6Al–4V alloy.
(7) Comparing the results of this study with the previous one showed that the patterned specimens have better electrochemical stability than the flat counterparts because of low wettability. Further studies on the biological compatibility of patterned specimens will be required for the application of fabricated biomaterials in implantology.

Declaration of Competing Interest

The authors do not declare competing interests. Aydin Bordbar-Khiabani reports receiving financial support provided by European Commission which is acknowledged below.

Acknowledgements

Financial supports of the European Union's Horizon 2020 research and innovation program under the Marie Skłodowska-Curie Action ITN "Premurosa" (GA 860462) are gratefully acknowledged. We also thankfully acknowledge the help and cooperation of Btech Innovations Ltd. in each stage of production of 3D-printed Ti layers.

Appendix A. Supplementary data

Supplementary data to this article can be found online at https://doi.org/10.1016/j.jmrt.2023.07.113.

REFERENCES

[1] Shah FA, Trobos M, Thomsen P, Palmquist A. Commercially pure titanium (cp-Ti) versus titanium alloy (Ti6Al4V) materials as bone anchored implants—is one truly better than the other? Mater Sci Eng C 2016;62:960–6.
[2] Kaur M, Singh K. Review on titanium and titanium based alloys as biomaterials for orthopaedic applications. Mater Sci Eng C 2019;102:844–62.
[3] Hanawa T. Biocompatibility of titanium from the viewpoint of its surface. Sci Technol Adv Mater 2022;23(1):457–72.
[4] Zhang LC, Chen LY. A review on biomedical titanium alloys: recent progress and prospect. Adv Eng Mater 2019;21(4):1801215.
[5] Gasik M, Braem A, Chaudhari A, Duyck J, Vleugels J. Titanium implants with modified surfaces: meta-analysis of in vivo osteointegration. Mater Sci Eng C 2015;49:152–8.
[6] Gasik M. Understanding biomaterial-tissue interface quality: combined in vitro evaluation. Sci Technol Adv Mater 2017;18(1):550–62.
[7] Depboylu FN, Yasa E, Poyraz Ö, Minguella-Canela J, Korkusuz F, De los Santos López MA. Titanium based bone implants production using laser powder bed fusion technology. J Mater Res Technol 2022;17:1408–26.
[8] Murr LE, Amato KN, Li SJ, Tian YX, Cheng XY, Gaytan SM, et al. Microstructure and mechanical properties of open-cellular biomaterials prototypes for total knee replacement implants fabricated by electron beam melting. J Mech Behav Biomed Mater 2011;4(7):1396–411.
[9] Lee Y, Jung A, Heo SJ, Gweon B, Lim D. Influences of surface topography of porous titanium scaffolds manufactured by powder bed fusion on osteogenesis. J Mater Res Technol 2023;23:2784–97.
[10] Gonçalves IM, Herrero ER, Carvalho O, Henriques B, Silva FS, Teughels W, et al. Antibiofilm effects of titanium surfaces modified by laser texturing and hot-pressing sintering with silver. J Biomed Mater Res B Appl Biomater 2021;109(10):1588–600.

[11] Xu Y, Liu W, Zhang G, Li Z, Hu H, Wang C, et al. Friction stability and cellular behaviors on laser textured Ti–6Al–4V alloy implants with bioinspired micro-overlapping structures. J Mech Behav Biomed Mater 2020;109:103823.
[12] Song P, Hu C, Pei X, Sun J, Sun H, Wu L, et al. Dual modulation of crystallinity and macro-/microstructures of 3D printed porous titanium implants to enhance stability and osseointegration. J Mater Chem B 2019;7(17):2865–77.
[13] Tiainen L, Abreu P, Buciumeanu M, Silva F, Gasik M, Guerrero RS, et al. Novel laser surface texturing for improved primary stability of titanium implants. J Mech Behav Biomed Mater 2019;98:26–39.
[14] Jing D, Zhai M, Tong S, Xu F, Cai J, Shen G, et al. Pulsed electromagnetic fields promote osteogenesis and osseointegration of porous titanium implants in bone defect repair through a Wnt/β-catenin signaling-associated mechanism. Sci Rep 2016;6(1):32045.
[15] Murr LE. Metallurgy principles applied to powder bed fusion 3D printing/additive manufacturing of personalized and optimized metal and alloy biomedical implants: an overview. J Mater Res Technol 2020;9(1):1087–103.
[16] Murr LE. Strategies for creating living, additively manufactured, open-cellular metal and alloy implants by promoting osseointegration, osteoinduction and vascularization: an overview. J Mater Sci Technol 2019;35(2):231–41.
[17] Miranda G, Faria S, Bartolomeu F, Pinto E, Alves N, Peixinho N, et al. A study on the production of thin-walled Ti6Al4V parts by selective laser melting. J Manuf Process 2019;39:346–55.
[18] Bartolomeu F, Carvalho O, Gasik M, Silva FS. Multi-functional Ti6Al4V-CoCrMo implants fabricated by multi-material laser powder bed fusion technology: a disruptive material's design and manufacturing philosophy. J Mech Behav Biomed Mater 2023;138:105583.
[19] Kwak TY, Yang JY, Heo YB, Kim SJ, Kwon SY, Kim WJ, et al. Additive manufacturing of a porous titanium layer structure Ti on a Co-Cr alloy for manufacturing cementless implants. J Mater Res Technol 2021;10:250–67.
[20] Wang X, Xu S, Zhou S, Xu W, Leary M, Choong P, et al. Topological design and additive manufacturing of porous metals for bone scaffolds and orthopaedic implants: a review. Biomaterials 2016;83:127–41.
[21] Itälä AI, Ylänen HO, Ekholm C, Karlsson KH, Aro HT. Pore diameter of more than 100 μm is not requisite for bone ingrowth in rabbits. J Biomed Mater Res 2001;58(6):679–83.
[22] Weißmann V, Bader R, Hansmann H, Laufer N. Influence of the structural orientation on the mechanical properties of selective laser melted Ti6Al4V open-porous scaffolds. Mater Des 2016;95:188–97.
[23] Gao C, Peng S, Feng P, Shuai C. Bone biomaterials and interactions with stem cells. Bone Research 2017;5(1):1–33.
[24] Scheinpflug J, Pfeiffenberger M, Damerau A, Schwarz F, Textor M, Lang A, et al. Journey into bone models: a review. Genes 2018;9(5):247.
[25] Zhao D, Huang Y, Ao Y, Han C, Wang Q, Li Y, et al. Effect of pore geometry on the fatigue properties and cell affinity of porous titanium scaffolds fabricated by selective laser melting. J Mech Behav Biomed Mater 2018;88:478–87.
[26] Taniguchi N, Fujibayashi S, Takemoto M, Sasaki K, Otsuki B, Nakamura T, et al. Effect of pore size on bone ingrowth into porous titanium implants fabricated by additive manufacturing: an in vivo experiment. Mater Sci Eng C 2016;59:690–701.
[27] Eliaz N. Corrosion of metallic biomaterials: a review. Materials 2019;12(3):407.
[28] Sasikumar Y, Indira K, Rajendran N. Surface modification methods for titanium and its alloys and their corrosion behavior in biological environment: a review. J Bio Tribo-Corrosion 2019;5:1–25.
[29] Yang J, Song Y, Dong K, Han EH. Research progress on the corrosion behavior of titanium alloys. Corrosion Rev 2023;41(1):5–20.
[30] Sadtler K, Singh A, Wolf MT, Wang X, Pardoll DM, Elisseeff JH. Design, clinical translation and immunological response of biomaterials in regenerative medicine. Nat Rev Mater 2016;1(7):1–7.
[31] Franz S, Rammelt S, Scharnweber D, Simon JC. Immune responses to implants–a review of the implications for the design of immunomodulatory biomaterials. Biomaterials 2011;32(28):6692–709.
[32] Carlander U, Midander K, Hedberg YS, Johanson G, Bottai M, Karlsson HL. Macrophage-assisted dissolution of gold nanoparticles. ACS Appl Bio Mater 2019;2(3):1006–16.
[33] Anderson JM, Rodriguez A, Chang DT. Foreign body reaction to biomaterials. Semin Immunol 2008;20(2):86–100.
[34] Mahlobo MG, Chikosha L, Olubambi PA. Study of the corrosion properties of powder rolled Ti–6Al–4V alloy applied in the biomedical implants. J Mater Res Technol 2022;18:3631–9.
[35] Bordbar-Khiabani A, Gasik M. Electrochemical and biological characterization of Ti–Nb–Zr–Si alloy for orthopedic applications. Sci Rep 2023;13(1):2312.
[36] Kuczyńska-Zemła D, Sotniczuk A, Pisarek M, Chlanda A, Garbacz H. Corrosion behavior of titanium modified by direct laser interference lithography. Surf Coating Technol 2021;418:127219.
[37] Zhang Q, Guan Y. Laser induced periodic surface structure on titanium alloy and its effect on microstructure refinement and corrosion behavior. J Alloys Compd 2023;936:168188.
[38] Kumari R, Pfleging W, Besser H, Majumdar JD. Microstructure and corrosion behavior of laser induced periodic patterned titanium based alloy. Opt Laser Technol 2019;116:196–213.
[39] Pede D, Li M, Virovac L, Poleske T, Balle F, Müller C, et al. Microstructure and corrosion resistance of novel β-type titanium alloys manufactured by selective laser melting. J Mater Res Technol 2022;19:4598–612.
[40] Hariharan A, Goldberg P, Gustmann T, Maawad E, Pilz S, Schell F, et al. Designing the microstructural constituents of an additively manufactured near β Ti alloy for an enhanced mechanical and corrosion response. Mater Des 2022;217:110618.
[41] Ahmadi S, Sadrnezhaad SK. A novel method for production of foamy core@compact shell Ti6Al4V bone-like composite. J Alloys Compd 2016;656:416–22.
[42] Van Bael S, Kerckhofs G, Moesen M, Pyka G, Schrooten J, Kruth JP. Micro-CT-based improvement of geometrical and mechanical controllability of selective laser melted Ti6Al4V porous structures. Mater Sci Eng: A. 2011;528(24):7423–31.
[43] Yan C, Hao L, Hussein A, Raymont D. Evaluations of cellular lattice structures manufactured using selective laser melting. Int J Mach Tool Manufact 2012;62:32–8.
[44] Vrancken B, Thijs L, Kruth JP, Van Humbeeck J. Heat treatment of Ti6Al4V produced by selective laser melting: microstructure and mechanical properties. J Alloys Compd 2012;541:177–85.
[45] Amaya-Vazquez MR, Sánchez-Amaya JM, Boukha Z, Botana FJ. Microstructure, microhardness and corrosion resistance of remelted TiG2 and Ti6Al4V by a high power diode laser. Corrosion Sci 2012;56:36–48.

[46] Melo-Fonseca F, Gasik M, Madeira S, Silva FS, Miranda G. Surface characterization of titanium-based substrates for orthopaedic applications. Mater Char 2021;177:111161.
[47] Saidi R, Raeissi K, Ashrafizadeh F, Kharaziha M. The effect of zinc oxide coating morphology on corrosion performance of Ti-6Al-4 V alloys. J Alloys Compd 2021;883:160771.
[48] Shaoki A, Xu JY, Sun H, Chen XS, Ouyang J, Zhuang XM, et al. Osseointegration of three-dimensional designed titanium implants manufactured by selective laser melting. Biofabrication 2016;8(4):45014.
[49] Dwivedi S, Dixit AR, Das AK, Adamczuk K. Additive texturing of metallic implant surfaces for improved wetting and biotribological performance. J Mater Res Technol 2022;20:2650–67.
[50] Acar MT, Kovacı H, Çelik A. Comparison of the structural properties, surface wettability and corrosion resistance of TiO_2 nanotubes fabricated on Cp-Ti, Ti6Al4V and Ti45Nb. Mater Today Commun 2022;33:104396.
[51] Asl HG, Sert Y, Küçükömeroğlu T, Bayrak Ö. The Comparison of wear performances of CP-Ti, Ti6Al4V, Ti45Nb alloys oxidized by anodic oxidation under ambient air and vacuum conditions. Mater Today Commun 2023;34:105466.
[52] Sotniczuk A, Kuczyńska-Zemła D, Kwaśniak P, Thomas M, Garbacz H. Corrosion behavior of Ti-29Nb-13Ta-4.6Zr and commercially pure Ti under simulated inflammatory conditions—comparative effect of grain refinement and non-toxic β phase stabilizers. Electrochim Acta 2019;312:369–79.
[53] Tengvall P, Elwing H, Lundström I. Titanium gel made from metallic titanium and hydrogen peroxide. J Colloid Interface Sci 1989;130(2):405–13.
[54] Hedberg YS, Gamna F, Padoan G, Ferraris S, Cazzola M, Herting G, et al. Surface modified Ti6Al4V for enhanced bone bonding ability—Effects of silver and corrosivity at simulated physiological conditions from a corrosion and metal release perspective. Corrosion Sci 2020;168:108566.
[55] Benea L, Simionescu-Bogatu N. Reactivity and corrosion behaviors of Ti6Al4V alloy implant biomaterial under metabolic perturbation conditions in physiological solutions. Materials 2021;14(23):7404.
[56] Pan J, Thierry D, Leygraf C. Electrochemical and XPS studies of titanium for biomaterial applications with respect to the effect of hydrogen peroxide. J Biomed Mater Res 1994;28(1):113–22.
[57] Stern M, Geary AL. Electrochemical polarization: I. A theoretical analysis of the shape of polarization curves. J Electrochem Soc 1957;104(1):56.
[58] Chen Y, Zhang J, Dai N, Qin P, Attar H, Zhang LC. Corrosion behaviour of selective laser melted Ti-TiB biocomposite in simulated body fluid. Electrochim Acta 2017;232:89–97.
[59] Prestat M, Vucko F, Holzer L, Thierry D. Microstructural aspects of Ti6Al4V degradation in H_2O_2-containing phosphate buffered saline. Corrosion Sci 2021;190:109640.
[60] Bai Y, Gai X, Li S, Zhang LC, Liu Y, Hao Y, et al. Improved corrosion behaviour of electron beam melted Ti-6Al–4V alloy in phosphate buffered saline. Corrosion Sci 2017;123:289–96.
[61] Al-Mobarak NA, Al-Mayouf AM, Al-Swayih AA. The effect of hydrogen peroxide on the electrochemical behavior of Ti and some of its alloys for dental applications. Mater Chem Phys 2006;99(2–3):333–40.
[62] Höhn S, Virtanen S. Effect of inflammatory conditions and H_2O_2 on bare and coated Ti–6Al–4V surfaces: corrosion behavior, metal ion release and Ca-P formation under long-term immersion in DMEM. Appl Surf Sci 2015;357:101–11.
[63] Metikos-Huković M, Kwokal A, Piljac J. The influence of niobium and vanadium on passivity of titanium-based implants in physiological solution. Biomaterials 2003;24(21):3765–75.
[64] Zhao B, Wang H, Qiao N, Wang C, Hu M. Corrosion resistance characteristics of a Ti-6Al-4V alloy scaffold that is fabricated by electron beam melting and selective laser melting for implantation in vivo. Mater Sci Eng C 2017;70:832–41.
[65] Morris D, Mamidi SK, Kamat S, Cheng KY, Bijukumar D, Tsai PI, et al. Mechanical, electrochemical and biological behavior of 3D printed-porous titanium for biomedical applications. J Bio Tribo-Corrosion 2021;7:1–5.
[66] Córdoba-Torres P, Mesquita TJ, Devos O, Tribollet B, Roche V, Nogueira RP. On the intrinsic coupling between constant-phase element parameters α and Q in electrochemical impedance spectroscopy. Electrochim Acta 2012;72:172–8.
[67] Brug GJ, van den Eeden AL, Sluyters-Rehbach M, Sluyters JH. The analysis of electrode impedances complicated by the presence of a constant phase element. J Electroanal Chem Interfacial Electrochem 1984;176(1–2):275–95.
[68] Ren S, Du C, Liu Z, Li X, Xiong J, Li S. Effect of fluoride ions on corrosion behaviour of commercial pure titanium in artificial seawater environment. Appl Surf Sci 2020;506:144759.
[69] Johnson WB, Macdonald JR. Fundamentals of impedance spectroscopy. In: Barsoukov E, Macdonald JR, editors. Impedance spectroscopy: theory, experiment, and applications. 2nd. ed. Hoboken, NJ: John Wiley & Sons, Inc.; 2005. p. 1–26.
[70] Lvovich VF. Impedance spectroscopy: applications to electrochemical and dielectric phenomena. John Wiley & Sons, Inc.; 2012. p. 37–47 [Chapter 3], Equivalent circuits modeling of the impedance phenomenon.
[71] Macdonald DD, McKubre MCH. Corrosion of materials. In: Barsoukov E, Macdonald JR, editors. Impedance spectroscopy: theory, experiment, and applications. 2nd. ed. Hoboken, NJ: John Wiley & Sons, Inc.; 2005. p. 343–429.
[72] Wang JL, Liu RL, Majumdar T, Mantri SA, Ravi VA, Banerjee R, et al. A closer look at the in vitro electrochemical characterisation of titanium alloys for biomedical applications using in-situ methods. Acta Biomater 2017;54:469–78.
[73] Qu Q, Wang L, Chen Y, Li L, He Y, Ding Z. Corrosion behavior of titanium in artificial saliva by lactic acid. Materials 2014;7(8):5528–42.
[74] Elshamy IH. Abd El Rehim SS, Ibrahim MA, El Boraei NF. The bifunctional role played by thiocyanate anions on the active dissolution and the passive film of titanium in hydrochloric acid. Corrosion Engineering. Sci Technol 2022;57(6):542–52.
[75] Li J, He Y, Shi W, Xiang S, Gao W. Different passivation behavior between α and β phases of Ti-6Al-4V in HCl solutions under oxygenated/deoxygenated conditions. Appl Surf Sci 2022;604:154539.
[76] Li R, Wu Z, Wangb Y, Ding L, Wang Y. Role of pH-induced structural change in protein aggregation in foam fractionation of bovine serum albumin. Biotechnol Reports 2016;9:46–52.
[77] Liamas E, Thomas OR, Muñoz AI, Zhang ZJ. Effect of the electrochemical characteristics of titanium on the adsorption kinetics of albumin. RSC Adv 2019;9(59):34265–73.
[78] Talha M, Ma Y, Kumar P, Lin Y, Singh A. Role of protein adsorption in the bio corrosion of metallic implants—a review. Colloids Surf B Biointerfaces 2019;176:494–506.
[79] Siddiqui MA, Ullah I, Liu H, Zhang S, Ren L, Yang K. Preliminary study of adsorption behavior of bovine serum albumin (BSA) protein and its effect on antibacterial and corrosion property of Ti-3Cu alloy. J Mater Sci Technol 2021;80:117–27.
[80] Mabilleau G, Bourdon S, Joly-Guillou ML, Filmon R, Baslé MF, Chappard D. Influence of fluoride, hydrogen peroxide and lactic acid on the corrosion resistance of commercially pure titanium. Acta Biomater 2006;2(1):121–9.

[81] Seo DI, Lee JB. Effects of competitive anion adsorption (Br- or Cl-) and semiconducting properties of the passive films on the corrosion behavior of the additively manufactured Ti-6Al-4V alloys. Corrosion Sci 2020;173:108789.
[82] Lu YJ, Liu XC, Liu YJ, Wu X, Jiang Y, Liu Z, et al. Corrosion behavior of novel titanium-based composite with engineering 3D artificial nacre-like structures. Compos Appl Sci Manuf 2023;164:107278.
[83] Berbel LO, Banczek ED, Karousis IK, Kotsakis GA, Costa I. Determinants of corrosion resistance of Ti-6Al-4V alloy dental implants in an in Vitro model of peri-implant inflammation. PLoS One 2019;14(1):e0210530.